Probing optically induced spin currents using terahertz spin waves in noncollinear magnetic bilayers

Tom Lichtenberg,[*] Maarten Beens, Menno H. Jansen, and Bert Koopmans

Department of Applied Physics, Eindhoven University of Technology, P.O. Box 513, 5600 MB Eindhoven, The Netherlands

Rembert A. Duine

Department of Applied Physics, Eindhoven University of Technology, P.O. Box 513, 5600 MB Eindhoven, The Netherlands
and Institute for Theoretical Physics, Utrecht University, Leuvenlaan 4, 3584 CE Utrecht, The Netherlands

Optically-induced spin currents have proven to be useful in spintronics applications, allowing for sub-ps all-optical control of magnetization. However, the mechanism responsible for their generation is still heavily debated. Here we use the excitation of spin-current induced THz spin-waves in noncollinear bilayer structures to study optically-induced spin currents in the time domain. We measure a significant laser-fluence dependence of the spin-wave phase, which can quantitatively be explained assuming the spin current is proportional to the time derivative of the magnetization. Measurements of the absolute spin-wave phase, supported by theoretical calculations and micromagnetic simulations, suggest that angular momentum transfer via the *s-d* interaction in combination with ballistic interlayer transport is sufficient to fully explain spin-current generation and transport in our experiments. Finally, we show that the damping-like optical STT dominates THz spin-wave generation. Our findings suggest laser-induced demagnetization and spin-current generation share the same microscopic origin.

I. INTRODUCTION

Sub-ps demagnetization of ferromagnets (FM) upon fs laser-pulse excitation has garnered a lot of attention since its discovery in 1996 by Beaurepaire *et al.* [1], both from a fundamental as well as a technological perspective. Over the past two decades, theoretical frameworks that describe this phenomenon in terms of local [2–4] and nonlocal [5] angular momentum dissipation have been developed. Concurrently, its great potential in future data storage application was first demonstrated with the discovery of all-optical magnetization switching in ferrimagnetic alloys [6].

The first experiments in collinear ferromagnetic bilayer structures showed that spin-angular momentum transfer between the two layers influenced both the speed and the magnitude of the laser-induced demagnetization of both layers [7]. In similar collinear systems, optically-induced spin currents have been used to enhance the efficiency and functionality of all-optical magnetization switching applications [8–10]. Studies of noncollinear bilayer systems have shown that optically-induced spin currents also allow for the control of the orientation of the magnetization [11–13]. In these experiments, the polarization of the generated spin current is (nearly) perpendicular to the local magnetization, so the injected spin current exerts an optically-induced spin-transfer torque (OSTT) on the magnetization. Recently, it was demonstrated that 90% of this spin current is absorbed within ~2 nm of the injection interface of the absorption layer, inducing a

significant inhomogeneity in the magnetization. This results in the sub-ps all-optical excitation of highly tunable standing spin-waves (SSW) with frequencies in the THz regime [14–16].

Optically-induced spin currents have been studied extensively in the last decade [5,17–29]. However, the physics governing their generation and transport is still heavily debated. Several mechanisms have been proposed. A first idea is based on the fact that upon laser excitation, mobile hot electrons are created in the FM. Battiato *et al.* suggested that this hot electron current is spin-polarized by the FM itself due to different lifetimes and velocities of excited majority and minority spins [5,30]. This results in a superdiffusive spin current flowing out of the FM, which contributes to the demagnetization process. A second possible mechanism, henceforth referred to as the *dM/dt* mechanism, is based on electron-magnon coupling. Here, the demagnetization is proposed to be due to magnon excitation, and the lost angular momentum is transferred to spin-polarized mobile conduction electrons, in accordance with angular momentum conservation [12,13]. The resulting spin current is thus directly proportional to the time derivative of the demagnetization. This implies laser-induced demagnetization acts as a source for spin-current generation out of the FM layer. In recent theoretical work, a microscopic interpretation of this mechanism was proposed. Any *dM/dt* leads to a splitting of the chemical potential of the s-electron system via so-called *s-d* scattering, providing a source for spin currents. In stark contrast to the superdiffusive model, optically excited hot electrons do not play a major role in the spin transport [31–33]. The role of hot electrons during laser-induced spin-current generation thus remains a subject of debate.

*t.lichtenberg@tue.nl

Literature suggests that the timescale and shape of the spin-current pulse depends on the excitation mechanism [12,13,26,34]. Additionally, the temporal profile of the generated spin currents is expected to scale differently with the laser-pulse energy, depending on the excitation mechanism. Specifically, increasing the laser-pulse energy leads to an increase of demagnetization times and thus a broadening of the temporal profile of the spin current pulse if the dM/dt mechanism is dominant [35,36]. Conversely, no such laser pulse energy dependence on the temporal profile of the spin current is expected if spin transport is dominated by primary excited hot electrons.

Spin currents are typically measured via spin accumulation in thick NM injection layers [12,13], optical second-harmonic generation [24] or by probing demagnetization induced THz radiation [37]. These methods respectively require long-distance transport or complex analysis in order to disentangle the spin current information, the demagnetization as well as artifacts, which typically show up while the system is in a highly non-equilibrium state (first few ps) [38–40]. We propose a complementary measuring scheme that circumvents these issues. We measure the phase of spin-current induced THz SSW in noncollinear structures with ultrathin spacer layers. This phase is directly related to the phase of the Fourier component of the spin-torque pulse at the frequency of the spin-wave, under the condition that the spin-current is absorbed completely. The advantage is that we can determine the phase with a sub-ps resolution well after the strongest non-equilibrium effects are over, i.e., without any contribution from magneto-optical artefacts that do not directly relate to the magnetization or spin accumulation. Also, by measuring the phase of the precessional signal at a frequency characteristic for the spin-receiving in-plane layer, we are sure to be only sensitive to the canting of that specific layer, and do not have to separate contributions from other layers. Thus, even though we cannot resolve the generated spin-current directly in the time domain, we have easy access to the Fourier components that give us pure information about the timescales involved with spin current generation.

In this paper, we study the timescales involved with laser-induced spin-current generation and transport. We do this by opposing the dM/dt mechanism to ballistic transport of optically-excited hot-electron spin-currents. We should stress that the latter mechanism is the simplest interpretation of hot-electron transport in our system, and any subtleties introduced by superdiffusion as well as the excitation of secondary hot electrons are not taken into account. Using the aforementioned measurement scheme, we observe a significant phase shift of the THz spin waves for increasing laser pulse energy, which is consistent with the dM/dt mechanism. A combination of calculations based on the s-d model and micromagnetic simulations corroborate these findings. Lastly, we measured the phase of the optically excited homogeneous mode to show that the measured dynamics are dominated by a damping-like torque.

II. SET-UP AND EXPERIMENTS

Our experiments are performed on a noncollinear bilayer structure consisting of SiB(substrate)/Ta(4)/
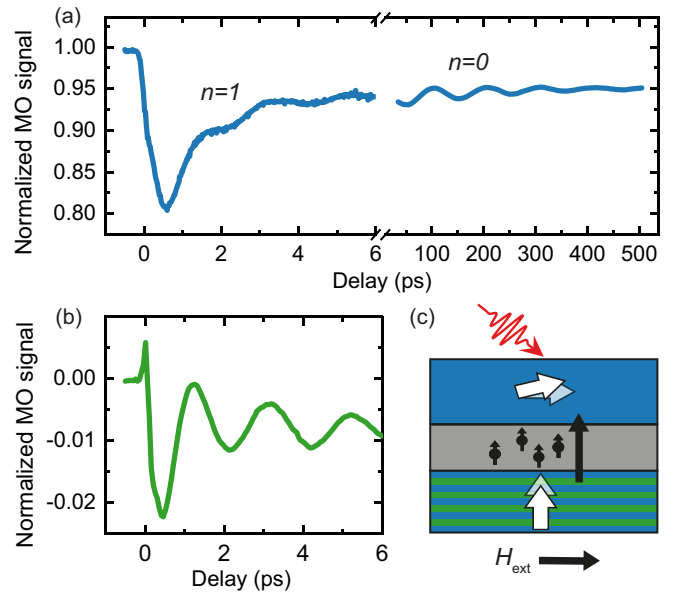

FIG. 1. (a) Normalized out-of-plane component of the measured magneto-optical (MO) signal of the magnetization dynamics of a noncollinear bilayer structure after fs laser-pulse excitation. The externally applied magnetic field is aligned in the plane and set to 0 and 91 mT respectively for the first-order inhomogeneous mode ($n = 1$) and the homogeneous mode ($n = 0$) measurements. Data normalization is discussed in Sec. I of the Supplemental Material [44]. (b) THz response of the absorption layer measured with Complex MOKE, normalized using the data in (a). A laser fluence of ≈ 2.7 mJ/cm^2 is used. (c) The sample geometry and OSTT mechanism.

Pt(4)/[Co(0.2)/Ni(0.6)]$_{4\times}$/Co(0.2)/Cu(2.5)/Co(5)/Pt(2.5) (thickness in brackets is indicated in nm), as grown by magneton sputtering. The stack, including relevant excitation mechanisms, is illustrated in Fig. 1(c). The Co/Ni multilayer is chosen for its PMA at relatively large magnetic volumes, making it an ideal thin film spin current generator [41,42]. This out-of-plane (OOP) magnetized layer is separated from an in-plane (IP) magnetized Co layer by a thin Cu spacer, which facilitates spin transport between the two magnetic layers after laser excitation. Upon laser excitation, both magnetic layers demagnetize, generating optically-induced spin currents. These spin currents are absorbed by the opposing layer, and are polarized perpendicularly to the local magnetization. As a consequence, the local magnetization cants due to the OSTT exerted by the spin currents, thereby exciting dynamics in the absorption layer. Due to the sizable PMA of the OOP layer, the spin current induced magnetization canting is suppressed, so the amplitude of any excited spin waves is typically below the noise threshold [15]. Therefore, the OOP and IP layer will henceforth also be referred to as the generation and absorption layer, respectively.

The laser-induced dynamics are measured using pump-probe spectroscopy, where the time-resolved magnetization is probed with the magneto-optical Kerr effect (MOKE). Laser pulses are generated by a Ti:sapphire laser at a repetition rate of 80 MHz and a wavelength of 780 nm. The pulse duration at sample position is in the order of 150 fs. Both pump and

probe pulses are focused onto the sample with a spot size of 16 and 8 μm respectively. The fluence dependence of the THz SSW properties are are measured for laser fluences between 1.2 and 2.6 mJ cm^{-2}. To extract pump-induced change of the magnetization, the pump beam is mechanically chopped at 60 Hz, while the polarization of the probe is modulated at 50 kHz by a photoelastic modulator. A dual lock-in scheme, locked to the two aforementioned frequencies, is used to measure the magneto-optical (MO) signal, and settings are chosen such that we are only sensitive to the Kerr rotation. The setup geometry is chosen such that the out-of-plane component of the Kerr rotation is probed. The sample is placed in a magnetic field of up to 180 mT, at a maximal angle of about 60° with the sample surface. We employ *complex MOKE* to filter out the magnetic response of the generation layer to improve the signal to noise ratio in our measurements [43]. Here, a quarter-wave plate (QWP) is included into the setup. Tuning the angle of the optical axis of the QWP rotates the Kerr vector in the complex plane, such that the magneto-optical information of a single layer can be filtered out in a crossed-polarizer setup. This allows for layer-specific measurements in bilayer systems.

III. EXPERIMENTAL RESULTS

A. Excitation of THz standing spin-wave modes

A typical magnetization trace is shown in Fig. 1(a). The OOP component of the magnetization of the complete stack, normalized to the decrease of the amplitude of the hysteresis loop, is plotted as a function of the delay of the probe pulse after pump pulse excitation. The data correspond to the superposition of the demagnetization dynamics of the OOP layer and the spin current induced dynamics of the IP layer. We refer to Sec. I of the Supplemental Material [44] for an explanation of the normalization process . On longer timescales and under the influence of an in-plane applied magnetic field, the spin current induced excitation of the ferromagnetic resonance mode ($n = 0$, $f \approx 10$ GHz) can be observed. On a sub-10 ps timescale we observe the inhomogeneous higher-order standing spin-waves, of which the first order SSW mode ($n = 1$) with a frequency of 0.48 ± 0.01 THz is clearly visible [14,15]. Because the spin current induces an inhomogeneous spin profile in the absorption layer, no magnetic fields are required to excite the SSW modes. Therefore, we measure them only at zero field. The response of the absorption layer after the implementation of *complex MOKE* is shown in Fig. 1(b). It should be noted that significant leakage of the filtered signal is unavoidable if it is large compared to the dynamics of interest, as is the case in our experiments. This leads to the complex behavior at small timescales and the general negative value of the measured signal.

B. THz standing spin-wave phase

In order to distinguish between the two aforementioned spin-current generation mechanisms, spin-current induced THz spin waves are measured as a function of laser fluence, from which the experimental fluence dependence of the spin-wave phase is extracted. These results are then compared to micromagnetic simulations where the expected fluence depen-

dence of the spin-wave phase is determined numerically for both mechanisms. In Figs. 2(a) and 2(b), the isolated fs laser-pulse-induced magnetic response of the OOP and IP layer are plotted respectively for various laser fluences. The demagnetization of the OOP layer, as displayed in Fig. 2(a), is fitted with an analytical solution of the phenomenological 3-temperature model (3TM) [45]. The spin-current-induced THz spin-waves are shown for various laser fluences in Fig. 2(b). As mentioned in the introduction, our measurements technique is only applicable if the incident spin current has been absorbed (almost) completely. To ensure this condition is met, only data delays larger than 2 ps are considered. An additional advantage of this approach is that the OOP is largely re-magnetized and signal intermixing in measurements where *Complex MOKE* is used is no longer an issue. To extract the spin-wave phase, a damped cosine function is used to fit the data after a global background subtraction. The delay at the first maximum of this fit is used to define the spin-wave phase, as indicated by the dashed line. This delay is plotted as a function of the normalized maximum demagnetization of the OOP layer in Fig. 2(e). A significant spin-wave phase shift as a function of demagnetization is observed, indicating that the changing demagnetization timescales significantly affect the temporal profile of the generated spin current.

C. Fluence dependence of the homogeneous mode

To acquire more information about the spin-wave excitation mechanism, the homogeneous mode is also measured as a function of laser fluence. The results, as shown in Fig. 3(a), indicate that for the entire studied fluence range, the first maximum of the fit corresponds to zero time delay within the margin of error, corresponding to a spin-wave phase shift of $(0 \pm 1)°$. In Sec. IV B we show how this outcome can be used to make a quantitative estimate of the relative importance of damping-like and field-like contributions to the spin-transfer torque.

IV. THEORY AND DISCUSSION

A. Interpretation of experimental results

To further investigate our results, we simulate the response of a one-dimensional IP magnetized layer after excitation with an OOP polarized spin current. We employ the MUMAX^3 package [46] to solve the LLG equation including the Slonczewski spin-transfer torque term and calculate the magnetic response. The spin current is assumed to exert a pure damping-like (DL) torque on the magnetization of the absorption layer [26,47]. The spin current absorption decays exponentially with a typical length scale of 0.96 nm, in accordance with Ref. [15]. We simulate the experimental laser attenuation with an exponential function using an attenuation coefficient of 13 nm [48]. Any enhanced MOKE effects at the interface with the Pt capping layer are neglected. Simulation and material parameters are discussed in detail in Sec. III of the Supplemental Material [44].

As previously mentioned, the temporal profile of the laser-pulse induced ballistic hot-electron spin current only depends on the excitation profile, i.e., the Gaussian laser pulse. Again,
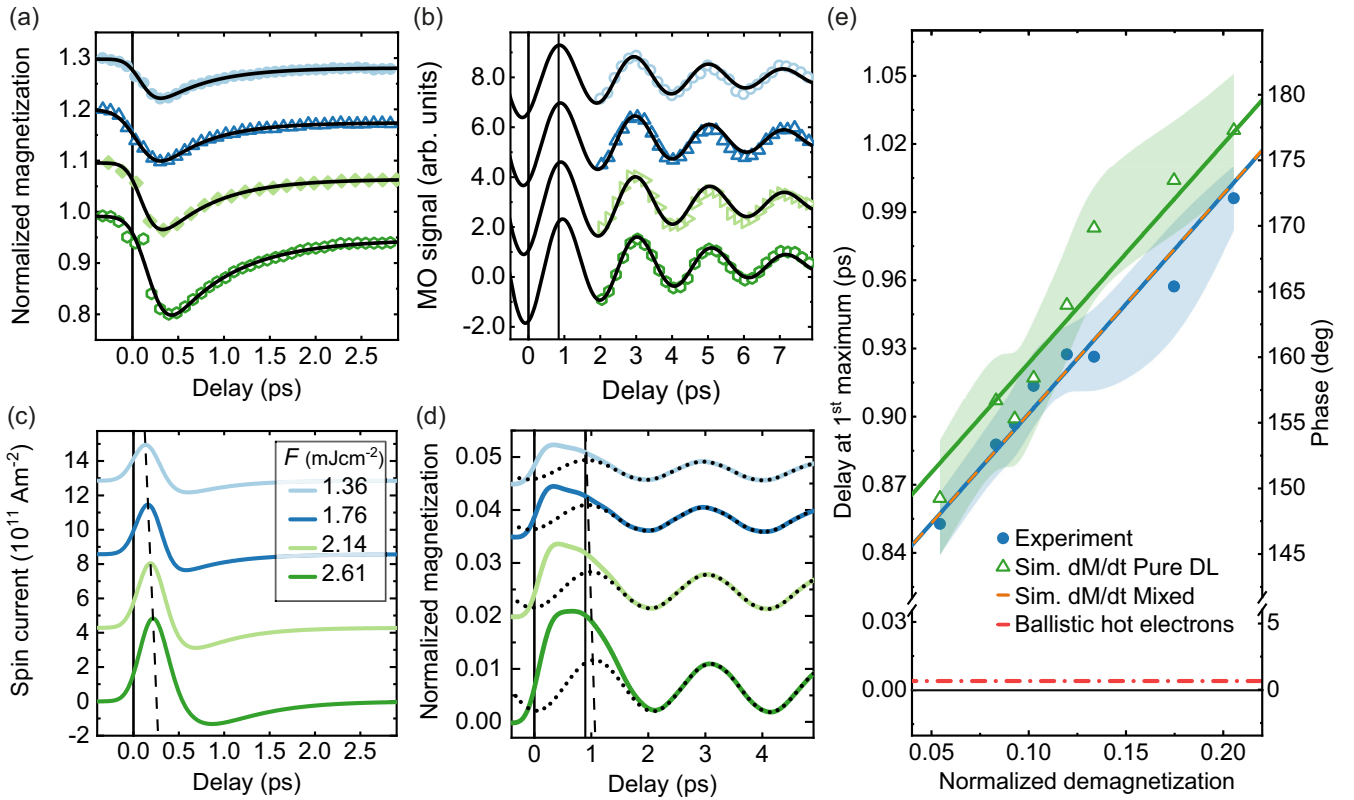
FIG. 2. (a) Normalized laser-induced demagnetization for 4 different laser fluences. Black lines indicate fits with the 3TM. Normalization is discussed Sec. I of the Supplemental Material [44]. (b) MOKE measurements of the OOP component of the IP layer magnetization, acquired using *Complex MOKE*, fitted with a damped cosine function in black. (c) The generated spin currents, calculated with Eq. (1). (d) Micromagnetic simulations of spin current induced dynamics in the absorption layer (OOP component). The dotted line indicates fits with a damped cosine function. The dashed lines provide a guide to the eye for the fluence dependencies. (e) The delay at the first maximum of the fit in (c) as a function of the normalized demagnetization extracted from the data in (a). The shaded areas and solid lines indicate the uncertainty regions and linear fits of the data with a shared slope. The dashed orange line indicates simulation results where a field-like contribution of 5.6% to the spin current induced torque is assumed. The red dot-dashed line corresponds to ballistic transport of optically excited hot electrons. Data presented in [(a)–(d)] are plotted with an arbitrary offset to improve visibility. See Sec. V of the Supplemental Material [44] for a full overview of the measurements and simulations.

we stress that this is only explicitly the case when considering primary excited hot electrons and disregarding the dynam-
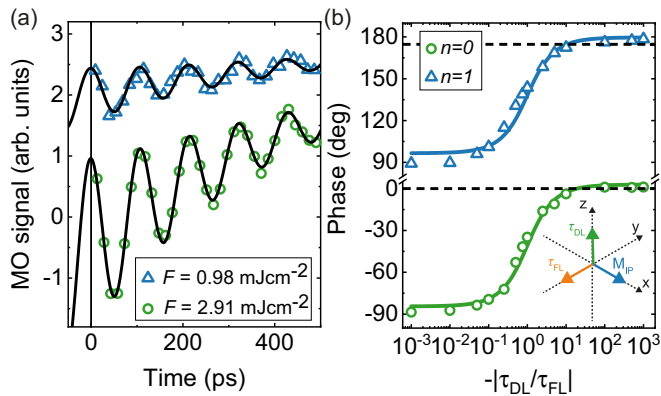

FIG. 3. (a) The homogeneous modes, at an in-plane magnetic field of 91 mT. (b) Simulated phase as a function of the ratio between FL and DL torque. The data is fitted with an arctangent and the dashed lines indicate experimental values.

ics of secondary electrons. In this case, the behavior of the spin-current induced spin waves is trivial; ballistic transfer of angular momentum leads to excited SSWs with a laser-fluence independent spin wave phase of (close to) zero degrees. Based on first-principle calculations of the Fermi velocity a phase shift in the order of $1°$ is expected [49].

In stark contrast to spin-polarized ballistic hot electron currents, spin currents generated with the dM/dt mechanism depend on the temporal profile of the demagnetization. Increasing the laser-pulse energy leads to an increase of the timescales associated with the demagnetization [35,36,50]. This influences the temporal profile of the generated spin current, and thus the spin-wave phase.

We use the *s-d* model in combination with transport models to calculate the spin current absorbed by the absorption layer [31–33]. Because the transverse spin coherence length of Co is smaller than the absorption layer thickness, it can be modelled as an ideal spin sink [15,51]. Furthermore, because the spacer layer is only 2.5 nm, we assume ballistic interlayer spin transfer between the two magnetic layers. Under these assumptions, the spin current absorbed by the absorption layer

(in units of Am^{-2}) can be written as

$$J_S = -\varepsilon \frac{e\, d_G M_{S,G}}{\mu_B} \frac{dm_G}{dt}. \tag{1}$$

Here, $d_G = 3.4$ nm, $M_{S,G} = 0.66$ MAm^{-1} [15] and m_G are the thickness, saturation magnetization and normalized magnetization of the generation layer respectively. e and μ_B are the electron charge and the Bohr magneton. Furthermore, ε denotes the spin transfer efficiency between the two layers, which results from the relative importance of spin transport to the bottom Pt and local spin relaxation due to for instance Elliot-Yaffet processes [35,44]. The full derivation of this equation is presented in Appendix A. In Appendix B we provide an in-depth comparison between ballistic and diffusive approach to interlayer transport. We show that both approaches yield similar results when applied to the noncollinear system studied in this paper, even though a diffusive model is not completely valid for electron transport on length scales below the mean free path it is not completely valid [5,52]. Even so, Eq. (1) remains a valid approximation regardless of the models used to describe interlayer transport.

In order to quantify the expected fluence dependence of the spin-wave phase in this scenario, we take the time derivative of the MOKE data presented in Fig. 2(a). It should be noted that transient changes of the magneto-optical constant due to optical excitations can potentially influence the MOKE signal [38,39], which lead to differences between measurement and the true demagnetization. In Sec. II of the Supplemental Material [44], we show that these effects are small and we can confidently use the data to determine dM/dt. The resulting spin current profiles, as calculated with Eq. (1), are plotted in Fig. 2(c), and used as the input for our micromagnetic simulations. The simulated response of the absorption layer is depicted in Fig. 2(d), with $\varepsilon \approx 0.06$ chosen such that the amplitude of the excited SSWs matches the experimental value. Our findings are in accordance with spin-transfer efficiency measurements done on our sample (see Sec. IV of the Supplemental Material [44]), which yield $\varepsilon = 0.068 \pm 0.009$, as well as literature (0.02–0.10) [11,15]. The sharp decrease of the amplitude after the first oscillation is attributed to the negative peak in the spin current, which corresponds to the remagnetization of the generation layer. For increasing laser fluence, the spin current amplitude increases and the temporal profile both broadens and shifts, leading to an increased spin-wave amplitude and phase, respectively. Again, a damped cosine function is used to fit the THz response for time delays larger than 2 ps. The delay at the first maximum of the fit is plotted as a function of the total laser induced demagnetization in Fig. 2(e). Here, the uncertainty is determined by both the 3TM fits in Fig. 2(a) and the damped cosine fit in Fig. 2(d). A significant time shift of ≈ 150 fs is observed as a function of laser fluence, corresponding to a phase shift of about 30°. This shift is attributed to the increase of the demagnetization times for increasing laser fluences, which leads to the shift of the spin current pulse as indicated in Fig. 2(c) with the dashed line. Within the error margin the measurements coincide with the simulations, which is consistent with a dominant dM/dt mechanism in our experiment. Furthermore, the agreement between the measured and simulated absolute

spin-wave phase suggests that an approach based on the *s-d* model in combination with instantaneous interlayer spin transfer suffices to describe our results completely. Literature suggests that similar phase shifts could also be expected due to laser-induced modulation of the exchange stiffness [53]. However, we discuss in Sec. VI of the Supplemental Material [44] why this is unlikely to be the case in our experiments.

B. Damping-like vs field-like torques

Up until this point, the absorbed spin current is assumed to exert a pure DL torque due to the OSTT on the absorption layer. Němec *et al.* showed that this is a sound assumption [54]. However, phase measurements of the THz spin waves allow us to study FL spin-transfer torque contributions in more detail and confirm this in our experiments. For this purpose, additional measurements of the homogeneous mode were done for two different laser fluences. We recapitulate that we measured a spin-wave phase of 0 ± 1 degree [Fig. 3(a)], which is shown as a horizontal dashed line in Fig. 3(b). MUMAX^3 has been employed to simulate the phase of both the homogeneous mode and the 1st order mode as a function of the ratio between the FL and DL spin-transfer torque [46]. Refer to Sec. VII of the Supplemental Material [44] for the simulation details. The results are plotted in Fig. 3(b). Because the FL torque points in the IP direction and the DL torque in the OOP direction, as sketched in the inset of Fig. 3(b), a 90-degree phase shift is expected when the FL torque becomes dominant. Comparing these simulations with our experimental results in Fig. 3(b), we can estimate the ratio of DL and FL torques from the point where the simulation curve crosses the horizontal line representing the experimentally determined phase. Thus, it can be concluded that the DL OSTT is dominant in our experiments, which is in line with our measurements of the THz spin waves, as well as previous theoretical considerations of spin current induced THz spin waves [26,47] and experiments using linearly polarized laser light [54–56]. Assuming a negative FL contribution of about 5.6%, the simulated and measured THz spin-wave phase completely overlaps, as indicated in Fig. 2(e), indicating a small FL component in our experiments. The ratio between the FL and DL torque is given by the ratio between the imaginary and real part of the spin-mixing conductance at the Cu/Co interfaces, which is typically small for a nonmagnetic/transition metal interface [57,58]. First-principle calculations of this ratio for Cu(1 1 1)/Co provide a value of 2.2-2.8% [59,60]. However, it should be noted that the observed systematic phase shift could be caused by other effects as well, such as a modulation of the shape of the current pulse due to for instance hot electron transport. Moreover, the measured shift is small, and just a little above the error margin. In conclusion, our detailed analysis confirms the dominance of the DL, and a possible FL component will not be larger than several percents.

V. CONCLUSION

We have shown that noncollinear bilayer structures are ideal tools to study the rich physics of fs laser-pulse-induced magnetization dynamics in magnetic multilayers. We

measured the optical spin-current-induced THz spin-wave phase as a function of laser fluence to study the temporal profile of the optically-induced spin current itself. We find that the THz spin-wave phase increases with increasing laser fluence, which is consistent with the notion that the optically-induced spin current is proportional to the time derivative of the laser-induced demagnetization. These results suggest that ultrafast demagnetization acts as a source of spin current generation in our experiments. We corroborate this finding using calculations based on the *s-d* model, where we derive this direct relation between generated spin current and laser-induced demagnetization. Furthermore, a combination of the *s-d* model and a simple ballistic interlayer transport picture is enough to fully explain both the relative phase shift as well as the absolute phase. In future research, a thorough treatment of the superdiffusive spin current generation model could further increase our understanding. Lastly, it has been shown that the DL OSTT-mechanism dominates spin transfer from the spin current to the local magnetization of the absorption layer.

ACKNOWLEDGMENTS

APPENDIX A: DERIVATION OF EQUATION (1)

Here we present the derivation of Eq. (1) from the main text. We define a spin current J_s (in units Am^{-2}), that describes the net (OOP polarized) spin flow from the OOP generation layer to the IP absorption layer. The longitudinal spin dynamics within the generation layer is described in terms of the spin accumulation μ_s [12,31,61]

$$\frac{d\mu_{s,G}}{dt} = \frac{1}{N_F} \frac{M_{s,G}}{\mu_B} \frac{dm_G}{dt} - \frac{\mu_{s,G}}{\tau_{s,G}} - \frac{J_s}{(-e)d_G N_F}, \quad (A1)$$

where the first term on the right-hand side corresponds to the source term arising from the local *s-d* interaction [12,31,32,61], with N_F the spin-averaged density of states at the Fermi level, $M_{s,G}$ the saturation magnetization of the generation layer, m is the normalized magnetization, e is the electron charge, and μ_B the Bohr magneton. The second term describes the spin-flip processes, parametrized by time scale $\tau_{s,G}$. The third term expresses the spins pumped out of the generation layer. The factor d_G^{-1}, with d_G the generation layer thickness, arises from the area to volume ratio.

We assume transport in the spacer (Cu) layer is ballistic. Then, the exchange of spin between the generation layer and absorption layer is determined by the difference in spin accumulation of the layers. This approach is similar to Sec. IV of Ref. [33]. Since the IP layer absorbs the spins with an OOP polarization very efficiently, we assume that the absorption layer acts as an ideal spin sink and set the spin accumulation (specifically, its OOP component) to zero $\mu_{s,A} = 0$. This yields the following expression for the interlayer spin current

$$J_s = (-e)\frac{G}{\hbar}\mu_{s,G}, \quad (A2)$$

where G is an effective conductance expressed in units m^{-2} and includes the electronic and spin-mixing conductance of both interfaces. Now we substitute this expression in Eq. (A1) and simplify

$$\frac{d\mu_{s,G}}{dt} = \frac{1}{N_F} \frac{M_{s,G}}{\mu_B} \frac{dm_G}{dt} - \frac{\mu_{s,G}}{\tau}, \quad (A3)$$

where we introduced the time scale $\tau^{-1} = \tau_{s,G}^{-1} + \tau_B^{-1}$ with definition $\tau_B^{-1} = G/(\hbar d_G N_F)$. The time scale τ functions as a response time. In the limit that τ is the shortest time scale in the system, which can correspond to either an ultrashort τ_B or $\tau_{s,G}$, the temporal profile of the spin accumulation will be directly determined by the source term. In this limit the spin accumulation is given by

$$\mu_{s,G} = \tau \frac{1}{N_F} \frac{M_{s,G}}{\mu_B} \frac{dm_G}{dt}. \quad (A4)$$

Substituting this back into Eq. (A2) yields

$$J_s = (-e)\frac{1}{\frac{\tau_B}{\tau_{s,G}}+1} \frac{d_G M_{s,G}}{\mu_B} \frac{dm_G}{dt}. \quad (A5)$$

Note that the prefactor describes the ratio between the local spin loss (by $\tau_{s,G}$) compared to the spins transported towards the absorption layer. To account for additional spin leakage, e.g., towards the neighboring Pt layer or spin-flip processes at the interfaces, we replace the prefactor by a phenomenological efficiency parameter ε. Then, the spin current is expressed as

$$J_s = \varepsilon \frac{(-e)d_G M_{s,G}}{\mu_B} \frac{dm_G}{dt}, \quad (A6)$$

which is Eq. (1) of the main text. This analytical approximation is valid as long as the response τ is relatively short. Explicit calculations are presented in Fig. 4, where we compare the spin current that follows from directly solving Eq. (A1) to the analytical approximation in Eqs. (A5) and (A6). We use the example source given by [12]

$$\frac{dm_G}{dt} = \left[A_1 \cdot \exp\left(-(t-t_1)^2/t_2^2\right) \right.$$
$$\left. + A_2 \cdot \exp\left(-(t-t_3)^2/t_4^2\right)\right], \quad (A7)$$

that describes the standard bipolar behavior. Here, $A_1 = 0.07$ ps^{-1}, $A_2 = -0.23$ ps^{-1}, $t_1 = 1.9\,ps$, $t_2 = 1.0\,ps$, $t_3 = 1.0\,ps$, and $t_4 = 0.2\,ps$.

Figure 4(a) presents the calculations for the material parameters that correspond to Ni (for the Co/Ni multilayer), summarized in Table I. We included a prefactor arranging the source term in units Am^{-2} [Eq. (A6) with $\varepsilon = 1.0$]. We find response time $\tau \sim 75$ fs [which leads to an additional 75 fs shift in the experiments presented in Fig. 2(e) in the main text] and efficiency $\varepsilon \sim 0.24$ [estimated via the prefactor in Eq. (A5)]. The calculations do not fully explain the experimental results, where no significant shift is observed, as well as a lower spin transfer efficiency. We argue that this discrepancy arises because we did not include the leakage of spins towards the Pt layer, and we do expect that the presence of multiple interfaces (as we have a Co/Ni multilayer and a Co/Pt interface) will effectively enhance the spin-flip relaxation rate. This can phenomenologically be introduced
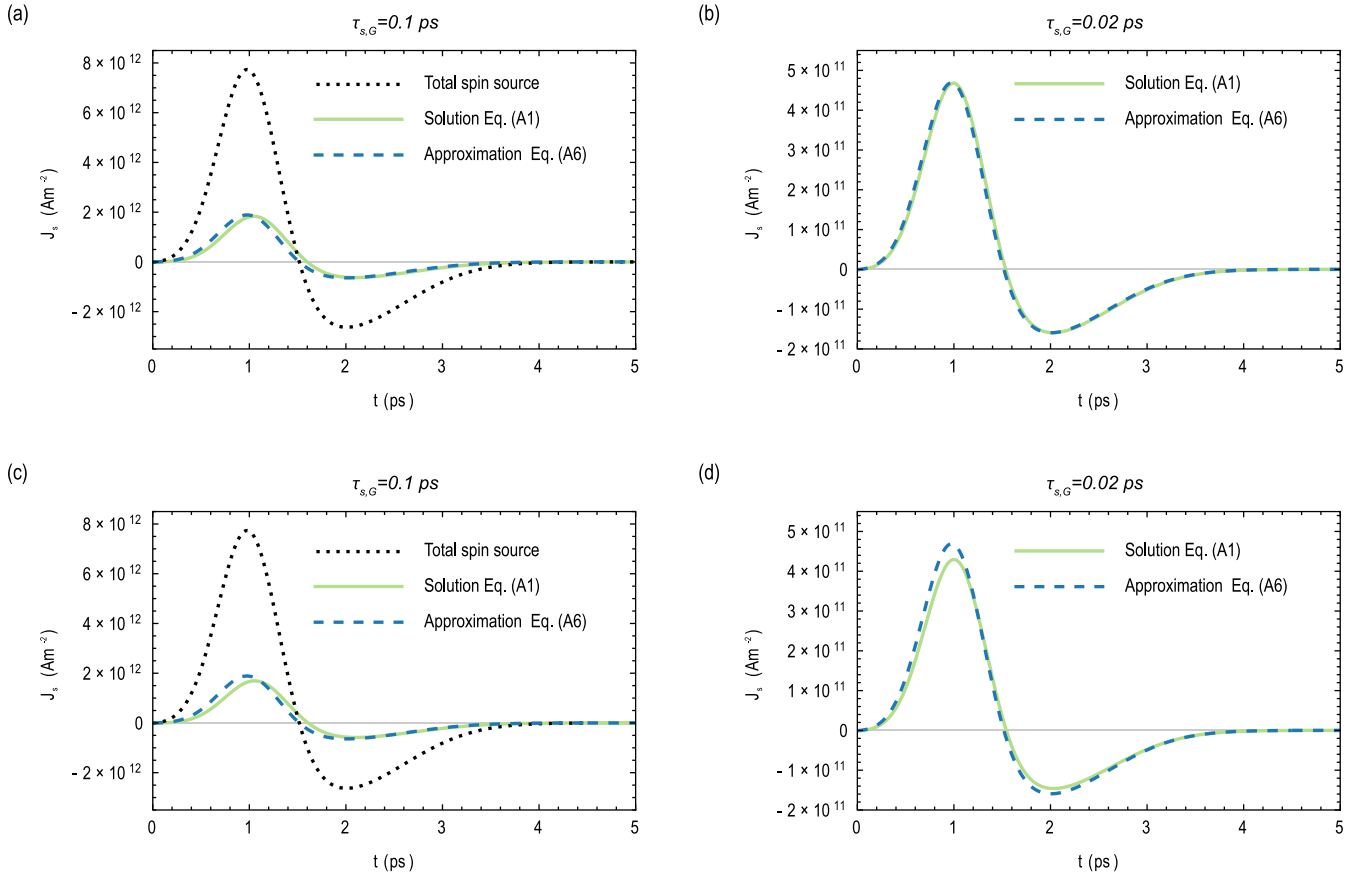
FIG. 4. Calculations of the interlayer spin current using a ballistic [(a)–(b)] and diffusive [(c)–(d)] description. (a) The ballistic calculation for the material constants of Ni. The black-dotted curve indicates the total spin source per unit area [Eq. (A6) with $\varepsilon = 1.0$]. The solid-green curve indicates the numerical result [solving Eq. (A1)]. The dashed-blue curve indicates the analytical approximation, as introduced in Eq. (A6). (b) Shows the ballistic calculation using an enhanced spin-flip scattering time of $\tau_{s,G} = 0.02$ ps. (c) The diffusive calculation for Ni, indicated by the solid green curve. (d) The diffusive calculation for $\tau_{s,G} = 0.02$ ps. Note that the subfigures have different scalings of the y axis.

TABLE I. Numerical values used in the calculations.

Symbol	Meaning	Estimate	Unit
μ_B	Bohr magneton	9.27×10^{-24}	Am^2
$M_{s,G}$	Saturation magnetization generation layer[a]	0.66×10^6	Am^{-1}
d_G	Generation layer thickness[a]	3.4	nm
d_{Cu}	Spacer layer thickness[a]	2.5	nm
$\tau_{s,Co/Ni}$	spin relaxation time Co/Ni[b]	0.1	ps
$\tau_{s,Co/Pt}$	spin relaxation time Co/Pt[b]	0.02	ps
σ_{Ni}	electrical conductivity Ni[b]	7.1×10^6	Sm^{-1}
σ_{Cu}	electrical conductivity Cu[b]	39×10^6	Sm^{-1}
D_{Ni}	diffusion coefficient Ni[b]	160	$nm^2 ps^{-1}$
D_{Cu}	diffusion coefficient Cu[b]	9500	$nm^2 ps^{-1}$
$N_{F,Ni}$	density of states Ni[c]	277	$eV^{-1} nm^{-3}$
$N_{F,Cu}$	density of states Cu[c]	26	$eV^{-1} nm^{-3}$
G	effective interface spin conductance[d]	0.2×10^{19}	m^{-2}

[a]Given in main text.
[b]Taken from [32].
[c]Calculated from the relation $D = \sigma / (e^2 N_F)$.
[d]Estimated via its relation to the interfacial electrical conductance $G = \hbar G_e / (2e^2)$ using the interfacial conductance G_e for a Co/Cu interface of $G_e = 2 \times 10^{15}$ Sm^{-2} [32]. For a single interface this yields, $G_{Co/Cu} = 0.4 \times 10^{19}$ m^{-2}. We estimate the effective G as two identical interfaces in series, which leads to an extra factor of $1/2$.

by using a shorter spin-flip relaxation time. For example, if we take the spin-flip time scale similar to that of a Co/Pt multilayer ($\tau_{s,G} = 0.02$ ps), an efficiency of $\varepsilon = 0.06$ is found, which is close to the experimental value. Furthermore, the shift is reduced to about 19 fs, which is within the margin of error in the experiments. Figure 4(b) shows the result for this enhanced spin-flip rate, suggesting a good correspondence between Eq. (A6) (limit $\tau \to 0$) and the complete solution. This supports the validity of an approach as presented in Eq. (1) of the main text and we conclude that a simple ballistic description suffices to explain the experimental implications. However, we stress that Eq. (A6) remains an approximation to the complete result, since the response time τ will always be finite.

APPENDIX B: BALLISTIC TRANSPORT VERSUS SPIN DIFFUSION

A similar result can be derived by solving the spin diffusion equation. The results are shown in Figs. 4(c) and 4(d). Although the simulation has similar results compared to the ballistic calculation in last section, we note that the validity of this diffusive approach is questionable for such small layer thicknesses. We here present a brief discussion of the diffusive approach, for details we refer to Ref. [33].

We define the OOP spatial coordinate x in the domain $x \in [-d_G, d_{Cu}]$. The interface between the generation layer and spacer layer is located at $x = 0$. The second interface is located at $x = d_{Cu}$. Beyond the second interface the spin accumulation is set to zero to simulate the absorption layer acting as an ideal spin sink. The spin current at $x = -d_G$ is set to zero. The continuity equation for the spins can be expressed

as [33,61]

$$
\frac{\partial \mu_s}{\partial t} = \frac{1}{N_F(x)} \frac{M_{s,G}}{\mu_B} \frac{dm_G}{dt}
$$
$$
+ \frac{1}{N_F(x)} \frac{\partial}{\partial x} \left(\frac{\sigma(x)}{e^2} \frac{\partial \mu_s}{\partial x} \right)
$$
$$
- \frac{\mu_s}{\tau_s(x)}, \tag{B1}
$$

where $\sigma(x)$ indicates the spin-averaged electrical conductivity and is a function of the spatial coordinate x. The source term is only nonzero in the ferromagnetic region. The interfacial spin current between the generation layer and spacer layer is expressed as

$$
J_{s,\mathrm{Co/Cu}}^{\mathrm{int}} = (-e) \frac{G_{\mathrm{Co/Cu}}}{\hbar} (\mu_s(0^-) - \mu_s(0^+)), \tag{B2}
$$

whereas the spin current into the sink (absorption layer) is given by

$$
J_s^{\mathrm{sink}} = (-e) \frac{G_{\mathrm{Co/Cu}}}{\hbar} \mu_s(d_{\mathrm{Cu}}^-). \tag{B3}
$$

The spin current J_s^{sink} resulting from the spin source [Eq. (A7)] is plotted in Figs. 4(c) and 4(d), for the same system parameters as the ballistic calculation. The figures show that the two calculations give similar results. This can be understood from the fact that the long spin diffusion length of the Cu layer leads to an approximately spatially constant spin current. Analogously to the ballistic calculation, changing the spin-flip relaxation time to the value for Co/Pt yields an efficiency that is close to the experimental value, as shown in Fig. 4(d).

[1] E. Beaurepaire, J.-C. Merle, A. Daunois, and J.-Y. Bigot, Phys. Rev. Lett. **76**, 4250 (1996).

[2] G. P. Zhang and W. Hübner, Phys. Rev. Lett. **85**, 3025 (2000).

[3] B. Koopmans, J. J. M. Ruigrok, F. Dalla Longa, and W. De Jonge, Phys. Rev. Lett. **95**, 267207 (2005).

[4] M. Djordjevic and M. Münzenberg, Phys. Rev. B **75**, 012404 (2007).

[5] M. Battiato, K. Carva, and P. M. Oppeneer, Phys. Rev. Lett. **105**, 027203 (2010).

[6] C. D. Stanciu, F. Hansteen, A. V. Kimel, A. Kirilyuk, A. Tsukamoto, A. Itoh, and T. Rasing, Phys. Rev. Lett. **99**, 047601 (2007).

[7] G. Malinowski, F. Dalla Longa, J. H. Rietjens, P. V. Paluskar, R. Huijink, H. J. Swagten, and B. Koopmans, Nat. Phys. **4**, 855 (2008).

[8] S. Iihama, Y. Xu, M. Deb, G. Malinowski, M. Hehn, J. Gorchon, E. E. Fullerton, and S. Mangin, Adv. Mater. **30**, 1804004 (2018).

[9] Y. L. W. van Hees, P. van de Meugheuvel, B. Koopmans, and R. Lavrijsen, Nat. Commun. **11**, 3835 (2020).

[10] Q. Remy, J. Igarashi, S. Iihama, G. Malinowski, M. Hehn, J. Gorchon, J. Hohlfeld, S. Fukami, H. Ohno, and S. Mangin, Adv. Sci. **7**, 2001996 (2020).

[11] A. J. Schellekens, K. C. Kuiper, R. R. J. C. De Wit, and B. Koopmans, Nat. Commun. **5**, 4333 (2014).

[12] G. M. Choi, B. C. Min, K. J. Lee, and D. G. Cahill, Nat. Commun. **5**, 4334 (2014).

[13] G.-M. Choi, C.-H. Moon, B.-C. Min, K.-J. Lee, and D. G. Cahill, Nat. Phys. **11**, 576 (2015).

[14] I. Razdolski, A. Alekhin, N. Ilin, J. P. Meyburg, V. Roddatis, D. DIesing, U. Bovensiepen, and A. Melnikov, Nat. Commun. **8**, 15007 (2017).

[15] M. L. M. Lalieu, P. L. J. Helgers, and B. Koopmans, Phys. Rev. B **96**, 014417 (2017).

[16] M. L. M. Lalieu, R. Lavrijsen, R. A. Duine, and B. Koopmans, Phys. Rev. B **99**, 184439 (2019).

[17] A. Melnikov, I. Razdolski, T. O. Wehling, E. T. Papaioannou, V. Roddatis, P. Fumagalli, O. Aktsipetrov, A. I. Lichtenstein, and U. Bovensiepen, Phys. Rev. Lett. **107**, 076601 (2011).

[18] D. Rudolf, L.-O. Chan, M. Battiato, R. Adam, J. M. Shaw, E. Turgut, P. Maldonado, S. Mathias, P. Grychtol, H. T. Nembach *et al.*, Nat. Commun. **3**, 1037 (2012).

[19] B. Vodungbo, J. Gautier, G. Lambert, A. B. Sardinha, M. Lozano, S. Sebban, M. Ducousso, W. Boutu, K. Li, B. Tudu *et al.*, Nat. Commun. **3**, 999 (2012).

[20] G.-M. Choi and D. G. Cahill, Phys. Rev. B **90**, 214432 (2014).

[21] J. Wieczorek, A. Eschenlohr, B. Weidtmann, M. Rösner, N. Bergeard, A. Tarasevich, T. O. Wehling, and U. Bovensiepen, Phys. Rev. B **92**, 174410 (2015).

[22] A. Eschenlohr, L. Persichetti, T. Kachel, M. Gabureac, P. Gambardella, and C. Stamm, J. Phys.: Condens. Matter **29**, 384002 (2017).

[23] M. Hofherr, P. Maldonado, O. Schmitt, M. Berritta, U. Bierbrauer, S. Sadashivaiah, A. Schellekens, B. Koopmans, D. Steil, M. Cinchetti, B. Stadtmüller, P. M. Oppeneer, S. Mathias, and M. Aeschlimann, Phys. Rev. B **96**, 100403(R) (2017).

[24] A. Alekhin, I. Razdolski, N. Ilin, J. P. Meyburg, D. Diesing, V. Roddatis, I. Rungger, M. Stamenova, S. Sanvito, U. Bovensiepen, and A. Melnikov, Phys. Rev. Lett. **119**, 017202 (2017).

[25] J. Hurst, P.-A. Hervieux, and G. Manfredi, Phys. Rev. B **97**, 014424 (2018).

[26] H. Ulrichs and I. Razdolski, Phys. Rev. B **98**, 054429 (2018).

[27] G. Zhang, Y. Bai, T. Jenkins, and T. F. George, J. Phys.: Condens. Matter **30**, 465801 (2018).

[28] J. K. Dewhurst, P. Elliott, S. Shallcross, E. K. Gross, and S. Sharma, Nano Lett. **18**, 1842 (2018).

[29] P. Baláž, M. Žonda, K. Carva, P. Maldonado, and P. M. Oppeneer, J. Phys.: Condens. Matter **30**, 115801 (2018).

[30] M. Battiato, K. Carva, and P. M. Oppeneer, Phys. Rev. B **86**, 024404 (2012).

[31] E. G. Tveten, A. Brataas, and Y. Tserkovnyak, Phys. Rev. B **92**, 180412(R) (2015).

[32] I.-H. Shin, B.-C. Min, B.-K. Ju, and G.-M. Choi, Jpn. J. Appl. Phys. **57**, 090307 (2018).

[33] M. Beens, R. A. Duine, and B. Koopmans, Phys. Rev. B **102**, 054442 (2020).

[34] D. M. Nenno, B. Rethfeld, and H. C. Schneider, Phys. Rev. B **98**, 224416 (2018).

[35] B. Koopmans, G. Malinowski, F. Dalla Longa, D. Steiauf, M. Fähnle, T. Roth, M. Cinchetti, and M. Aeschlimann, Nat. Mater. **9**, 259 (2010).

[36] K. Kuiper, T. Roth, A. Schellekens, O. Schmitt, B. Koopmans, M. Cinchetti, and M. Aeschlimann, Appl. Phys. Lett. **105**, 202402 (2014).

[37] R. Rouzegar, L. Brandt, L. Nadvornik, D. Reiss, A. Chekhov, O. Gueckstock, C. In, M. Wolf, T. Seifert, P. Brouwer *et al.*, arXiv:2103.11710.

[38] B. Koopmans, M. Van Kampen, J. Kohlhepp, and W. De Jonge, Phys. Rev. Lett. **85**, 844 (2000).

[39] I. Razdolski, A. Alekhin, U. Martens, D. Bürstel, D. Diesing, M. Münzenberg, U. Bovensiepen, and A. Melnikov, J. Phys.: Condens. Matter **29**, 174002 (2017).

[40] H. Eichler, D. Langhans, and F. Massmann, Opt. Commun. **50**, 117 (1984).

[41] H. Kurt, M. Venkatesan, and J. Coey, J. Appl. Phys. **108**, 073916 (2010).

[42] M. Johnson, P. Bloemen, F. Den Broeder, and J. De Vries, Rep. Prog. Phys. **59**, 1409 (1996).

[43] A. Schellekens, N. De Vries, J. Lucassen, and B. Koopmans, Phys. Rev. B **90**, 104429 (2014).

[44] See Supplemental Material at http://link.aps.org/supplemental/10.1103/PhysRevB.105.144416 for (i) further experimental de-tails and a discussion on temporal pump-probe overlap [62] (ii) a discussion of transient changes to the magneto-optical constants and acoustic modes [63], (iii) and overview of simulation and material parameters [64], (iv) experimental determination of the spin transfer efficiency, (v) a full overview of the fluence measurements, (vi) a discussion about the temperature dependence of the exchange stiffness [65] and (vii) further elaboration of field-like and damping like torque contributions.

[45] F. Dalla Longa, J. Kohlhepp, W. De Jonge, and B. Koopmans, Phys. Rev. B **75**, 224431 (2007).

[46] A. Vansteenkiste, J. Leliaert, M. Dvornik, M. Helsen, F. Garcia-Sanchez, and B. Van Waeyenberge, AIP Adv. **4**, 107133 (2014).

[47] U. Ritzmann, P. Baláž, P. Maldonado, K. Carva, and P. M. Oppeneer, Phys. Rev. B **101**, 174427 (2020).

[48] P. Johnson and R. Christy, Phys. Rev. B **9**, 5056 (1974).

[49] D. Gall, J. Appl. Phys. **119**, 085101 (2016).

[50] N. Moisan, G. Malinowski, J. Mauchain, M. Hehn, B. Vodungbo, J. Lüning, S. Mangin, E. E. Fullerton, and A. Thiaville, Sci. Rep. **4**, 4658 (2014).

[51] T. Taniguchi, S. Yakata, H. Imamura, and Y. Ando, IEEE Trans. Magn. **44**, 2636 (2008).

[52] S. Brorson, J. Fujimoto, and E. Ippen, Phys. Rev. Lett. **59**, 1962 (1987).

[53] U. Atxitia, D. Hinzke, O. Chubykalo-Fesenko, U. Nowak, H. Kachkachi, O. N. Mryasov, R. F. Evans, and R. W. Chantrell, Phys. Rev. B **82**, 134440 (2010).

[54] P. Němec, E. Rozkotová, N. Tesařová, F. Trojánek, E. De Ranieri, K. Olejník, J. Zeman, V. Novák, M. Cukr, P. Malý *et al.*, Nat. Phys. **8**, 411 (2012).

[55] G.-M. Choi, A. Schleife, and D. G. Cahill, Nat. Commun. **8**, 15085 (2017).

[56] G.-M. Choi, J. H. Oh, D.-K. Lee, S.-W. Lee, K. W. Kim, M. Lim, B.-C. Min, K.-J. Lee, and H.-W. Lee, Nat. Commun. **11**, 1482 (2020).

[57] M. Charilaou, K. Lenz, and W. Kuch, J. Magn. Magn. Mater. **322**, 2065 (2010).

[58] Y. Tserkovnyak, A. Brataas, G. E. W. Bauer, and B. I. Halperin, Rev. Mod. Phys. **77**, 1375 (2005).

[59] K. Xia, P. J. Kelly, G. E. W. Bauer, A. Brataas, and I. Turek, Phys. Rev. B **65**, 220401 (2002).

[60] M. Zwierzycki, Y. Tserkovnyak, P. J. Kelly, A. Brataas, and G. E. W. Bauer, Phys. Rev. B **71**, 064420 (2005).

[61] J. Kimling and D.G. Cahill, Phys. Rev. B **95**, 014402 (2017).

[62] C.-W. Luo, Y. Wang, F. Chen, H. Shih, and T. Kobayashi, Opt. Express **17**, 11321 (2009).

[63] W. Martienssen and H. Warlimont, *Springer Handbook of Condensed Matter and Materials Data* (Springer Science & Business Media, New York, 2006)

[64] C. A. F. Vaz, J. Bland, and G. Lauhoff, Rep. Prog. Phys. **71**, 056501 (2008).

[65] M. Krauß, T. Roth, S. Alebrand, D. Steil, M. Cinchetti, M. Aeschlimann, and H.C. Schneider, Phys. Rev. B **80**, 180407(R) (2009).